ARTICLE

Single Manganese Atom Anchored on N-doped Graphene as a Promising Catalyst for Nitrogen Reduction Reaction: A First-Principles Study

Li Xu, Yong Tang, Mengge Cao, Kuan Zhou, Hongbao Li*

Institutes of Physical Science and Information Technology, Key Laboratory of Structure and Functional Regulation of Hybrid Materials (Ministry of Education); Anhui Graphene Engineering Laboratory, Anhui University, Hefei 230601, China

(Dated: Received on March 16, 2024; Accepted on May 8, 2024)

Electrochemical synthesis of ammonia represents a green and environmentally friendly method distinct from traditional Harper-Bosch processes, which demand stringent conditions. However, identifying a catalyst with high selectivity and catalytic activity to cleave the robust triple bond of N_2 remains a formidable challenge. Herein, we present a systematic study on the geometrical and electronic structure, intensity of N_2 adsorption, reaction intermediates, change in Gibbs free energy, and desorption of by-product hydrazine for the nitrogen reduction reaction employing a MnN_x-graphene ($x = 3$, 4) catalyst from a theoretical perspective. The computational results reveal that MnN_3-graphene exhibits superior catalytic performance predominantly via the distal mechanism, with a low potential of 0.49 V. Moreover, the detachment of the produced NH_3 is facilitated with a free energy of only 0.27 eV, significantly lower than those of previous catalysts, ensuring the exceptional durability of MnN_3-graphene. This study offers theoretical insights guiding the exploration of single Mn atom catalysts in ammonia synthesis.

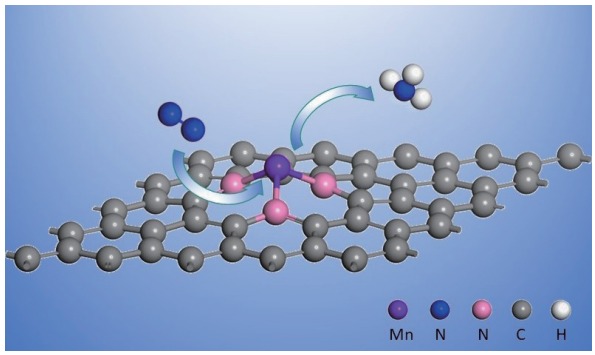

Key words: Manganese, N-doped graphene, Nitrogen reduction reaction

I. INTRODUCTION

Ammonia serves as a pivotal chemical raw material due to its versatile applications in the production of nitric acid, chemical fertilizers, plastics, and explosives [1–3]. Nitrogen, constituting the predominant gas (78%) in the atmosphere, presents abundant resources of ammonia synthesis for fertilizer production [4–7]. However, the formidable potential barrier imposed by the N≡N triple bond (945 kJ/mol) renders nitrogen challenging to be directly harnessed [8–11].

In nature, Azotobacter has the capability to reduce N_2 to NH_3 under ambient conditions. However, this process exhibits a slow reaction rate and prolonged cycles, rendering it impractical for meeting industrial demands [12, 13]. Currently, over 90% of the world's ammonia fertilizers are produced via the Haber-Bosch (HB) process. Nonetheless, this method necessitates stringent conditions including high temperature and pressure, leading to significant energy consumption and environmental pollution [14–17]. In recent years, inspired by the ammonia synthesis mechanism of nitrogenase, electrochemical synthesis of ammonia at room temperature and pressure has emerged as a prominent research focus [18–20]. The electrochemical N_2 reduction reaction (NRR) is a 6-electron and 6-proton pro-

* Author to whom correspondence should be addressed.
E-mail: lihb@mail.ustc.edu.cn

cess, involving multiple intermediates and reaction pathways [21, 22]. It can be conducted under mild conditions with low energy consumption and offers the potential for increased yield by controlling reaction parameters and environmental factors [23, 24]. Consequently, the design of an efficient NRR electrocatalyst under ambient conditions presents a significant challenge [25–27].

Pure metals and transition metal nanoclusters have been extensively utilized as catalysts in studies concerning ammonia synthesis reactions [28–31]. However, the high costs associated with precious metals and the poor stability of molecular catalysts utilizing these metals as reaction centers hinder their widespread adoption in large-scale industrial applications. In recent decades, the emergence of single-atom catalytic technology and the discovery of novel two-dimensional materials such as graphene, have garnered attention towards the potential application prospects of graphene-based single-metal catalysts [32–35].

Li *et al.* proposed a novel catalyst, FeN_3-embedded graphene, demonstrating the significance of the highly spin-polarized FeN_3 center in enhancing N_2 adsorption, activating the inert N≡N triple bond, and catalyzing the conversion of N_2 to ammonia [36]. Ling *et al.* explored the potential of experimentally synthesized single-atom catalysts, specifically single metal atoms (Cu, Pd, Pt, and Mo) loaded on nitrogen-doped carbon, for N_2 fixation [37]. Their predictions indicated that the Mo_1-N_1C_2 catalyst exhibits remarkable performance with a lower overpotential of 0.24 V. In our previous study, based on experimental observations, we proposed the MnN_4@ nanotube catalyst for catalyzing NRR through the alternating mechanism rather than the distal process [38]. While theoretical predictions align well with experimental measurements, doubts about the reliability of the conclusion persist primarily due to its non-periodic model. Conversely, Gao *et al.* theoretically investigated the catalytic performances of single-atom Mn catalysts supported by N-doped graphene substrates ($Mn_{SA}@V_x$-N_y, x=s, d. y=0, 1, 2, 3, 4) [39]. They asserted that $Mn_{SA}@V_s$-N_1 is the most promising candidate for NRR due to its high catalytic activity and selectivity. However, their conclusion may lack accuracy and rigor as only two out of the eleven types of single-atom Mn catalysts which were considered for the reaction calculation, and the free energy barrier of the potential determining step was found to be notably high (0.77 eV).

In this study, inspired by the prior research, we studied two catalytic configurations based on graphene, characterized by a different number of N atoms surrounding the Mn atom, denoted as MnN_x-graphene (x=3, 4). We analyze their structural stability, N_2 adsorption capacity, energy changes during the reaction, and associated charge variations. Our results indicate that, compared to MnN_4-graphene, MnN_3-graphene exhibits superior N_2 capture efficiency and catalytic activity in facilitating the NRR process, achieving an overpotential of only 0.33 V.

II. COMPUTATIONAL DETAILS

The interaction and exchange correlation energy between electrons and ions were characterized using the projector augmented wave (PAW) method and the Perdew-Burke-Ernzerhof (PBE) exchange-correlation functional [40–43]. A cutoff energy of 500 eV for the plane-wave basis set was employed. Spin-polarized calculations were utilized for all systems [44, 45]. Additionally, the DFT-D3 method was employed to describe van der Waals interactions [46]. The convergence criterion for the residual force was set to 0.01 eV/Å and 10^{-5} eV during structure relaxation.

To simulate the MnN_3-graphene, a single Mn atom anchored in 5×5×1 supercell graphene with a N atom doped near the Mn atom was used. For MnN_4-graphene, we eliminated two C atoms in the center of the surface of 5×5×1 super graphene, added a Mn in the hole, and replaced four C atoms around Mn with N atoms. A vacuum layer of 15 Å was built to model the catalyst surface, which was enough to avoid the interaction between two periodic units. The Brillouin zone was sampled with the Monkhorst-Pack mesh with a 5 × 5 × 1 k-point grid.

The adsorption energy (E_{ads}) is commonly used to access the adsorption capability of catalyst surfaces for reactants. The more negative the E_{ads}, the stronger the adsorption of intermediates on the catalyst surface, indicating greater stability of the adsorption structure, and thus facilitating electrocatalytic reactions. The formula for calculating the adsorption energy of N_2 is defined as:

$$E_{ads}(^*N_2) = E_{^*N_2} - E_* - E_{N_2} \quad (1)$$

where $E_{ads}(^*N_2)$ represents the adsorption energy of N_2, $E_{^*N_2}$ denotes the total energy of the system containing

DOI: 10.1063/1674-0068/cjcp2403036

N_2, $E*$ stands for the total energy of the catalyst surface, and E_{N_2} indicates the total energy of N_2.

The Gibbs free energy change (ΔG) in electrocatalytic nitrogen reduction is calculated based on the computational hydrogen electrode (CHE) model proposed by Nørskov *et al.* [47, 48]. In this method, at the condition of pH=0, T=298.15 K, pressure of 1 atm, no external potential applied, half the free energy of hydrogen in the gaseous state is equal to that of a proton and electron pair. According the CHE model, ΔG is defined as:

$$\Delta G = \Delta E + \Delta \mathrm{ZPE} - T\Delta S + eU + \Delta G_{\mathrm{pH}} \quad (2)$$

where ΔE is the electronic energy difference before and after the adsorption of reaction intermediates, ΔZPE represents changes in zero-point energies, and ΔS represents the change in entroy. ΔZPE and ΔS can be calculated using vibrational frequencies obtained from normal-mode analysis through density functional theory (DFT) calculations. For free molecules, the entropies is taken from the NIST database [49]. T represents the temperature, which is set to 298.15 K in this work. e and U denote the number of electrons transferred and the electrode potential applied, respectively. ΔG_{pH} is the pH correction, defined as

$$\Delta G_{\mathrm{pH}} = 2.303 \times k_{\mathrm{B}} \times T \times \mathrm{pH}$$

where k_{B} is the Boltzmann constant and the pH value is set to zero. The overpotential (η) of the reaction is calculated by:

$$\eta = U_{\mathrm{equilibrium}} - U_{\mathrm{limiting}}$$

where $U_{\mathrm{equilibrium}}$ is the equilibrium potential of NRR (−0.16 V) and U_{limiting} is the limiting potential computated by $U_{\mathrm{limiting}} = -\Delta G_{\mathrm{max}}/e$ (ΔG_{max} is the most positive ΔG, usually near the rate-determing step). All calculations were performed using the Vienna *ab initio* simulation package (VASP) [50, 51].

III. RESULTS AND DISCUSSION

A. Adsorption and activation of N_2 on MnN_x-graphene

Initially, we constructed two ideal theoretical models: MnN_4-graphene and MnN_3-graphene. In the former, double vacancy substitution was implemented, where the surrounding four carbon atoms were replaced by nitrogen, and the two middle carbon atoms were substituted by a single manganese atom. In contrast, for the latter, single vacancy substitution was employed, wherein the three surrounding carbon atoms were substituted by nitrogen, and only one manganese atom replaced the central carbon atom.

The distinct substitution strategies resulted in notable differences between the two optimized substrates. As illustrated in FIG. 1 (a) and (d), MnN_4-graphene maintains a planar structure overall. In contrast, MnN_3-graphene exhibits a clearly elevated central substitution region compared to the surrounding carbon surface. This observation is consistent with the literature's depiction of FeN_3 structure [36]. Additionally, the distance between manganese and nitrogen (Mn−N) is significantly reduced (Δd = 0.12 Å) in MnN_3-graphene compared to MnN_4-graphene.

Next, our focus shifts to the selectivity of N_2 adsorption, as it plays a crucial role in the cleavage of the N≡N triple bond and subsequent NRR reactions. In our study, the MnN_x (x=4, 3) site serves as a prominent reactive center in both theoretical models, and N_2 predominantly exhibits two adsorption patterns on the single atom Mn catalyst: end-on and side-on [37, 52]. We investigated the feasibility of these two adsorption patterns on the theoretical models. For MnN_4-graphene, as depicted in FIG. 1 (b) and (c), despite numerous attempts, optimization efforts consistently yielded only the end-on adsorption pattern. Conversely, in MnN_3-graphene, as shown in FIG. 1 (e) and (f), both adsorption patterns were found to coexist stably.

From FIG. 1, it is evident that in the end-on pattern, the Mn−N bond length increased on both substrates, particularly pronounced for MnN_3-graphene, where it increased from 1.79 Å to 1.94 Å. The N≡N bond length and the newly formed Mn−N bond length absorbed on the two substrates are very similar. The primary distinction lies in the orientation of N_2 adsorption: on the MnN_4-graphene surface, N_2 is nearly vertically adsorbed, whereas on MnN_3-graphene, it forms an angle of approximately 46° with the surface. In the side-on pattern, the Mn−N bond length on MnN_3-graphene increased from 1.79 Å to 2.03 Å, and the bond length between the Mn atom and the absorbed N_2 exceeded 2 Å. However, for MnN_4-graphene, only one nitrogen atom formed a 2.26 Å Mn−N bond with manganese, while the other nitrogen atom remained unbound, unable to form a standard side-on structure.

Regarding adsorption energy, the calculated values for the end-on and side-on patterns on MnN_4-graphene

DOI: 10.1063/1674-0068/cjcp2403036

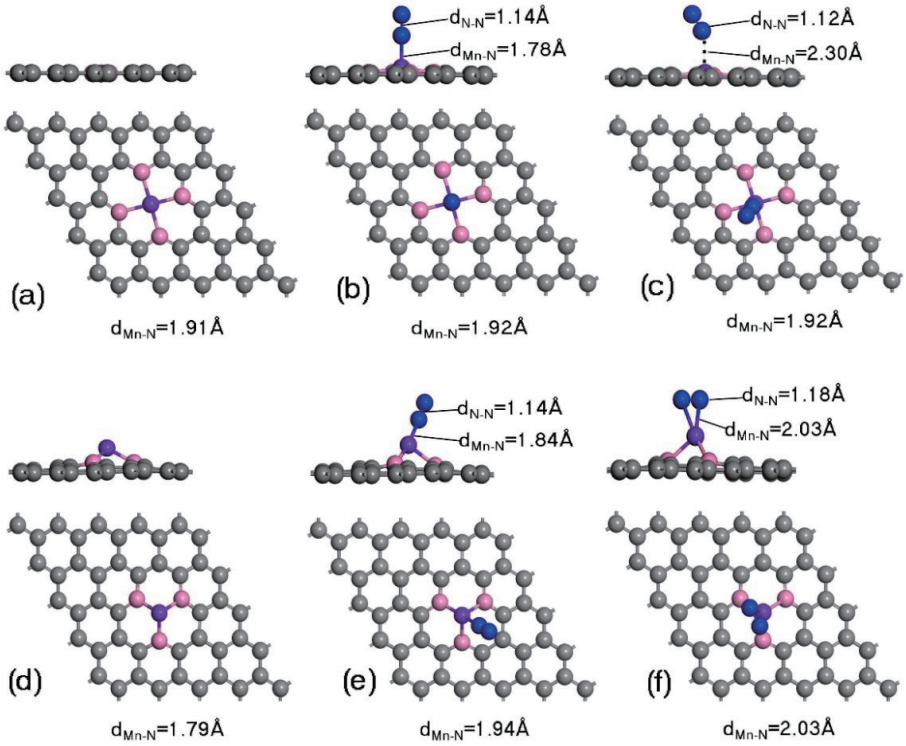

FIG. 1 Top and side views of structures of (a) MnN_4-graphene model. MnN_4-graphene with N_2 adsorption through (b) end-on and (c) side-on patterns. (d) MnN_3-graphene model. MnN_3-graphene with N_2 adsorption through (e) end-on and (f) side-on patterns. Gray, blue, pink, and purple balls represent the C, adsorbed N, doped N, and Mn atoms, respectively.

are −0.13 and −0.17 eV, respectively. However, for MnN_3-graphene, due to the greater structural changes before and after N_2 absorption, the adsorption energies for these two patterns increased to −1.32 and −1.41 eV, respectively. The adsorption effects of both of them are very close, with a numerical difference of only 0.09 eV. These differences in bond length, adsorption pattern, and binding energy further suggest that MnN_3-graphene may serve as a more favorable theoretical model compared to the MnN_4-graphene model employed in previous study [34].

FIG. 2 illustrates the projected density of states (PDOS) diagrams corresponding to the two substrates and different N_2 adsorption patterns. From FIG. 2 (a) and (d), it is evident that a strong interaction exists between the Mn and N atoms near the Fermi level in both substrates. Additionally, the Fermi level crossing the density of states (DOS) indicates that both substrates possess semiconductor properties. Upon N_2 adsorption, a significant interaction between the N-2p (in adsorbed N_2) and Mn-3d orbitals at the Fermi level is observed for the MnN_3-graphene model, whereas for the MnN_4-graphene model, this interaction is much weaker.

We further calculated the charge density electron local function (ELF) and the electron density difference maps corresponding to the two different N_2 adsorption models on different substrates. FIG. 3(a)−(d) illustrate the ELF of N_2 adsorption in different patterns. It is observed that after N_2 adsorption, regardless of the adsorption mode, the highest degree of electron localization is concentrated on the N atom far away from the surface. This concentration benefits the subsequent hydrogenation reaction, as the hydrogen atom is more inclined to react with this N atom. The differential charge reflects the electron transfer before and after N_2 adsorption. As shown in FIG. 3(e)−(g) for the MnN_4-graphene structure, electrons mainly gather on the Mn atom and four N atoms. In the end-on pattern, electrons are transferred from the MnN_4 group to the adsorbed N_2 group, and some electrons also aggregate between Mn and N atoms. In the side-on pattern, electrons are also present on the N atoms, but the far distance between N_2 and the substrate is not conducive to the next reaction step. From FIG. 3(h)−(j) for the MnN_3-graphene structure, electrons are mainly concentrated on the Mn atom and three N atoms. In the end-on pattern, electrons are transferred from MnN_3 to N_2, but there are almost no electrons on the Mn atom at this time. In the side-on

DOI: 10.1063/1674-0068/cjcp2403036

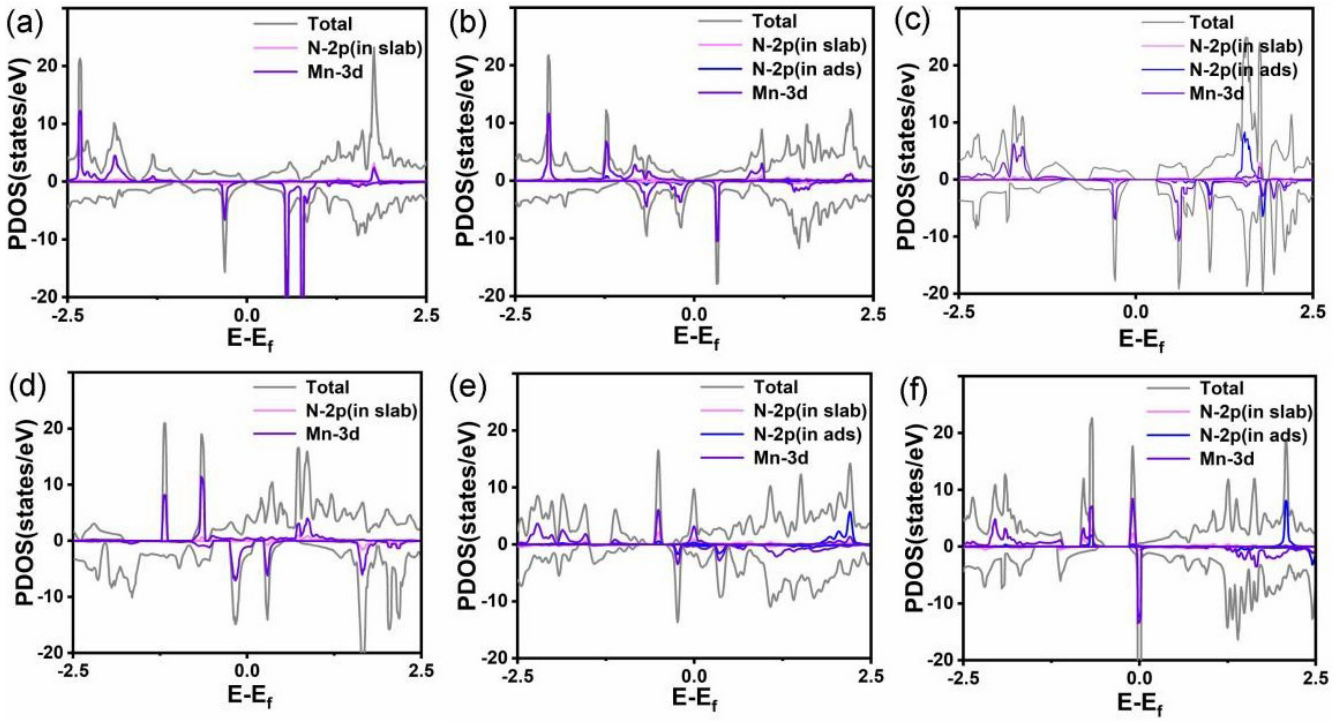

FIG. 2 PDOS for (a) MnN_4-graphene. PDOS of MnN_4-graphene with adsorption of N_2 through (b) end-on and (c) side-on patterns. PDOS for (d) MnN_3-graphene. PDOS of MnN_3-graphene with adsorption of N_2 through (e) end-on and (f) side-on patterns.

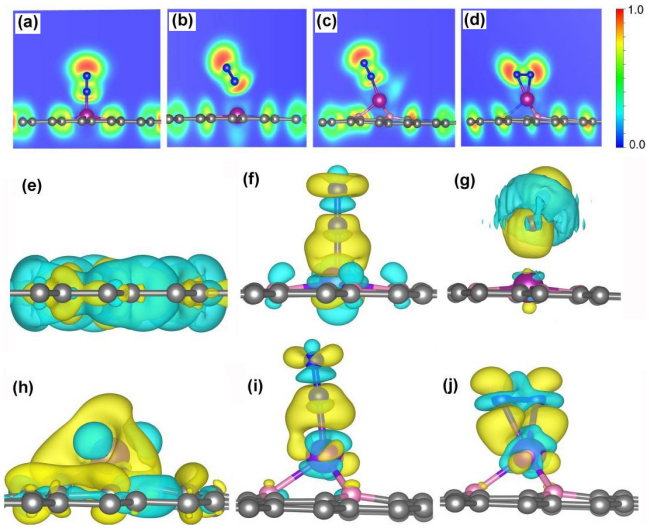

FIG. 3 ELF of MnN_4-graphene after adsorption of N_2 through (a) end-on and (b) side-on patterns. ELF of MnN_3-graphene after adsorption of N_2 through (c) end-on and (d) side-on patterns. Electron density difference of (e) MnN_4-graphene model and the absorption of N_2 on MnN_4-graphene through (f) end-on and (g) side-on patterns. Electron density difference of (h) MnN_3-graphene model and the absorption of N_2 on MnN_3-graphene through (i) end-on and (j) side-on patterns. The isosurface value is set to be 0.003 e/Å^3.

pattern, electrons transfer to the two N atoms, resulting in an increase in charge density, laying the foundation for the next reaction step.

The calculations of the Bader charge transfer in the N_2 adsorption process also support our previous analysis. For the MnN_4-graphene structure, the end-on adsorption pattern results in a charge transfer of 0.32 e to the N_2 molecules. Conversely, for the MnN_3-graphene structure, both the end-on and side-on patterns lead to a higher charge transfer of 0.34 e and 0.52 e to the N_2 molecule, respectively.

B. Reaction mechanism and Gibbs free energy diagram

Based on the structure, properties, and N_2 adsorption energy differences of the two constructed models, we selected the MnN_3-graphene model for the N_2 reduction to NH_3 reaction due to its higher potential. Generally, for the two different N_2 adsorption patterns, there are two possible catalytic pathways for each pattern: the distal and alternating mechanisms correspond to the end-on pattern, while the consecutive and enzymatic mechanisms correspond to the side-on pattern. In both the distal and consecutive mechanisms, the proton-electron pairs initially attack the N atom in the N_2 molecule that is the farthest from the surface and exhibits the highest degree of electron localization, resulting in the formation of NH_3. Subsequently, the remain-

DOI: 10.1063/1674-0068/cjcp2403036

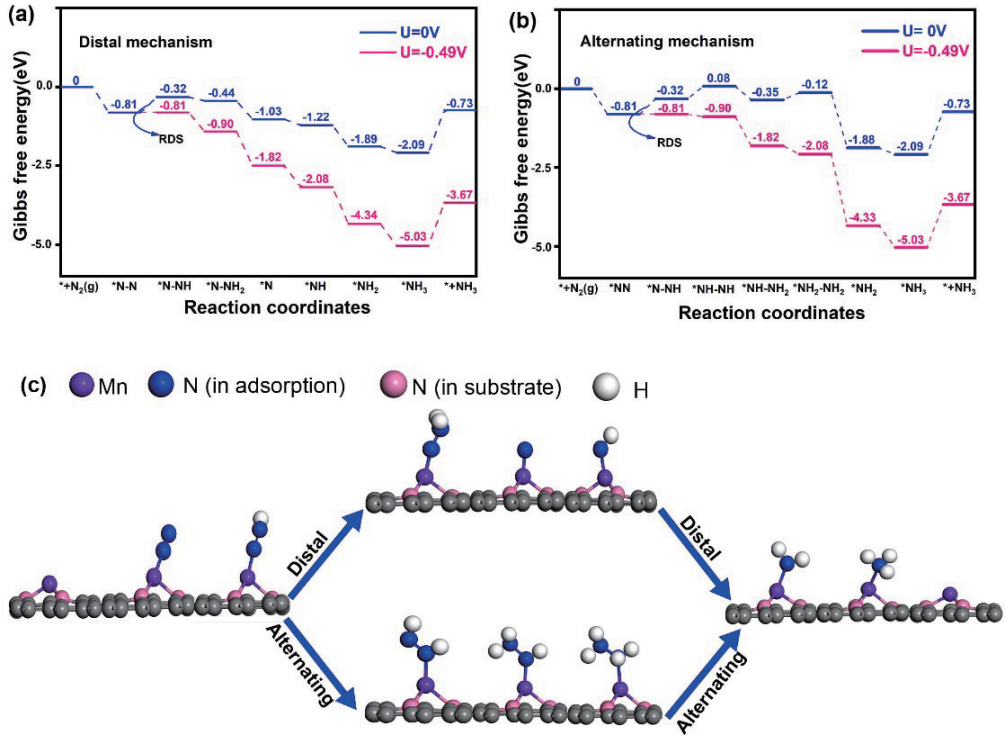

FIG. 4 Gibbs free energy diagrams for N_2 reduction on MnN_3-graphene with end-on adsorption mode by the (a) distal and (b) alternating mechanisms at different applied potentials, as well as (c) the corresponding structures of the reaction intermediates. Gray, blue, pink and purple balls represent the C, adsorbed N, doped N, and Mn atoms, respectively.

ing N atom is attacked to form another NH_3 molecule. On the other hand, in the alternating and enzymatic mechanisms, the proton-electron pairs sequentially attack these two N atoms until NH_3 is finally desorbed.

FIG. 4 illustrates the distal and alternating reactive mechanisms, along with the geometrical structures of the reaction intermediates, under the end-on adsorption mode on the MnN_3-graphene substrate. The process involves the adsorption and hydrogenation of N_2 in the first two steps to form $*N_2H$, followed by the hydrogenation of NH_2 to NH_3 and the desorption of the substrate in the last two steps. These steps remain consistent across both mechanisms, with the only variation occurring in the middle three steps. Due to the strong adsorption capacity of the substrate (as shown in FIG. 1(e)), the Gibbs free energy change before and after the first step of N_2 adsorption is significant (−0.81 eV), indicating that the MnN_3-graphene substrate efficiently captures N_2. The second step involves the hydrogenation of $*N_2$ to $*N_2H$, which is an endothermic process requiring energy consumption, with a change in free energy of 0.49 eV. This step serves as the rate-determining step for both reaction mechanisms, and the energy change is notably smaller than the value (0.77 eV) reported in the previous literature based on $Mn_{SA}@V_S$-N_1 [39]. The calculated overpotential value is 0.33 V, considerably lower than that of most metal catalysts (greater than 0.50 V) [53]. This low overpotential demonstrates the excellent catalytic performance of the MnN_3-graphene substrate in NRR.

FIG. 5 illustrates the NRR free energy diagram and the corresponding geometry of reaction intermediates for N_2 reduction in the side-on mode on the MnN_3-graphene substrate. The free energy change of N_2 adsorption at the first step remains highly negative (−1.00 eV), even lower than that in the end-on mode, ensuring effective capture of N_2 and activation of the N≡N triple bond. However, in the subsequent step, the free energy change for the hydrogenation of adsorbed N_2 to N_2H is approximately 0.68 eV for both mechanisms, significantly higher than the corresponding value (0.49 eV) of the end-on mode. This step also serves as the rate-determining step for both conservative and enzymatic mechanisms. Despite the smaller change in free energy at this step compared to previous result (0.77 eV) [39], the calculated overpotential is 0.52 V. Although the side-on mode on MnN_3-graphene exhibits slightly better performance than the single-atom Mn

DOI: 10.1063/1674-0068/cjcp2403036

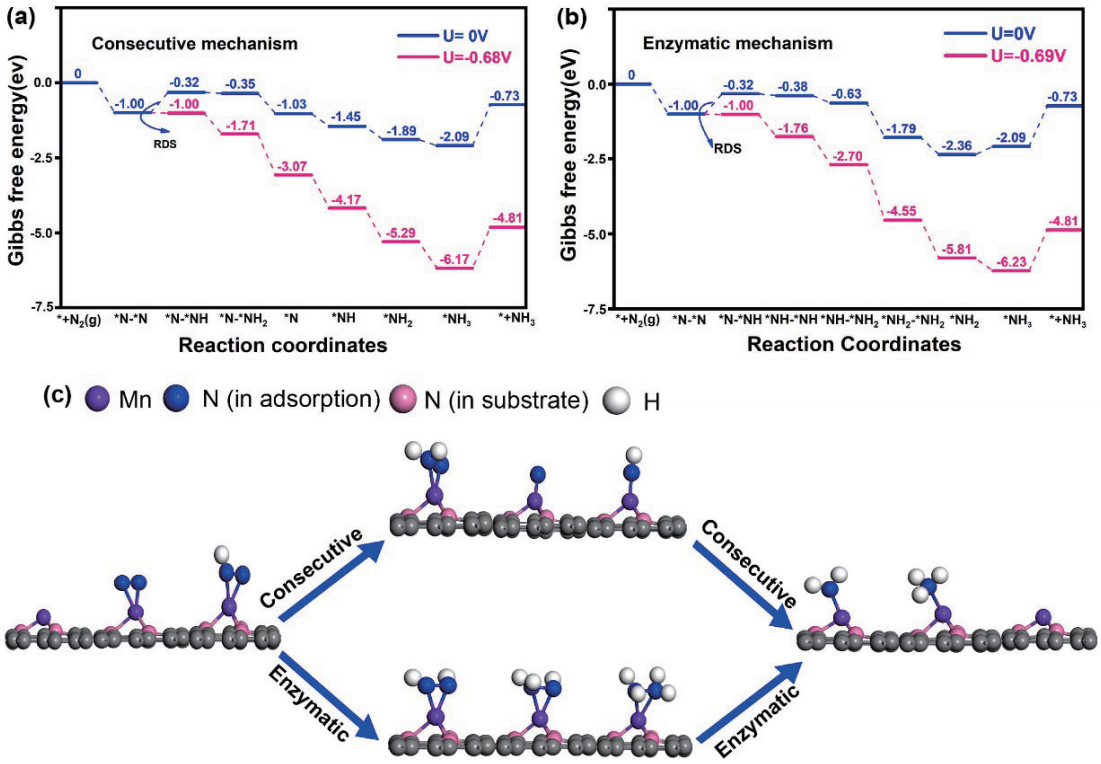

FIG. 5 Gibbs free energy diagrams for N_2 reduction on MnN_3-graphene with side-on adsorption mode by (a) consecutive and (b) enzymatic mechanisms at different applied potentials, as well as (c) the corresponding structures of the reaction intermediates. Gray, blue, pink and purple balls represent the C, adsorbed N, doped N and Mn atoms, respectively.

catalyst in previous literature [39], it is less efficient compared to the end-on mode.

We also computed the NRR reaction free energy diagrams corresponding to the end-on mode on the MnN_4-graphene substrate. As depicted in FIG. S1 (Supplementary materials, SM), it is evident that the adsorption of N_2 in the first step is an endothermic reaction, requiring 0.38 eV of energy consumption. In the subsequent step, which also serves as the rate-determining step, the free energy barrier for the hydrogenation of N_2 to N_2H is notably high at 0.84 eV, even exceeding the previous results. The calculated overpotential is 0.68 V, further underscoring the limited catalytic efficacy of this configuration.

Overall, compared to MnN_4-graphene and the previously recommended $Mn_{SA}@V_S$-N_1 in the literature, the low overpotential and high reactivity of the MnN_3-graphene model position it as a more ideal single-atom Mn catalyst for NRR [39].

In addition to possessing excellent electrochemical activity, an ideal catalyst should also exhibit high selectivity towards the NRR reaction. Competitive hydrogen evolution reaction (HER) reactions often occur during the NRR reaction, thus, an ideal NRR catalyst must not only demonstrate high NRR activity but also effectively suppress HER. The first step of the NRR reaction involves the adsorption of N_2 on the catalyst surface. In the presence of competitive HER reactions, H atoms adsorb onto the catalyst surface, occupying the active sites and hindering N_2 adsorption, thereby affecting the efficiency of the NRR reaction. Therefore, we evaluated the competition between NRR and HER by computing the values of $E_{ads}(*H)$ and $E_{ads}(*N_2)$. For catalysts with high NRR selectivity, when $E_{ads}(*N_2) < E_{ads}(*H)$, N_2 adsorption is more favorable for the NRR process, whereas when $E_{ads}(*N_2) > E_{ads}(*H)$, HER is favored. The formula for calculating the adsorption energy ($E_{ads}(*H)$) of H atom on the Mn-N_x-graphene surface is provided in the footnote of Table S1 (SM). Upon calculation, we found that for MnN_4-graphene, $E_{ads}(*N_2) < E_{ads}(*H)$, while for MnN_3-graphene, $E_{ads}(*N_2) < E_{ads}(*H)$. This indicates that both MnN_4-graphene and MnN_3-graphene can effectively suppress competitive HER and exhibit outstanding catalytic activity towards NRR.

The exceptional performance of metal single-atom

DOI: 10.1063/1674-0068/cjcp2403036

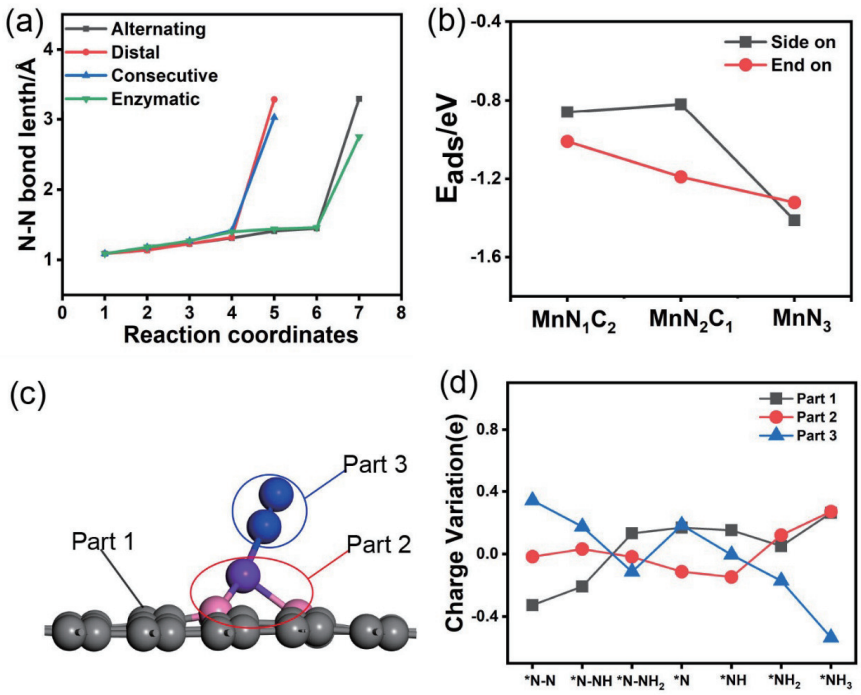

FIG. 6 (a) Changes of N–N bond length in the four reaction mechanisms. (b) Comparison of the adsorption energy of Mn-N_x-graphene (x=1, 2, 3). (c) Division of three parts in the intermediate product. (d) Bader charge variation in the distal mechanism.

NRR catalysts is not only closely tied to the N_2 adsorption energy and the free energy barrier at the rate-determining step, but also determined by the potential changes in intermediates and the difficulty of NH_3 desorption. Among the various reaction pathways based on the MnN_3-graphene model, two reactions potentially involve N_2H_4 desorption: $*NH_2NH_2 = * + N_2H_4$ in the alternating mechanism and $*NH_2*NH_2 = * + N_2H_4$ in the enzymatic mechanism. In Table S2, we computed the changes in free energy and adsorption energy under these two modes. From the adsorption energy data (−1.92 and −3.57 eV), it is evident that in both modes, N_2H_4 can strongly adsorb onto the substrate Mn single atom, making desorption into hydrazine N_2H_4 at room temperature implausible.

In Table S3 (SM), we conducted calculations on the free energy changes of the two NH_3 desorption processes generated during the four types of reaction pathways. In most cases, desorption of the first NH_3 molecule occurs readily, particularly in the distal mechanism, where its free energy change during desorption is only 0.27 eV. This value is considerably lower than that reported in the literature [39], underscoring its stability and durability, and suggesting it as the predominant reaction pathway. Additionally, in the end-on mode, despite the strong adsorption energy (1.32 eV), the free energy change associated with NH_3 desorption on MnN_3-graphene is very low, indicating the ease of NH_3 desorption under these conditions. Consequently, the MnN_3-graphene model is highly likely to serve as an NRR catalyst with excellent stability.

To provide robust support for future experimental investigations, we conducted further analyses on the significant effects of changes in the N–N bond length from adsorption to activation and fracture, alterations in coordination environments, and variations in charge distribution throughout different stages of the reaction process on single Mn atom catalysts. In FIG. 6(a), we analyzed the N–N bond length changes across four reaction pathways. It is observed that during the transition from the gaseous state of N_2 (step 1) to gradual hydrogenation, the bond length exhibits a linear increase, resembling previous NRR calculations [37]. This suggests a stable equilibrium between adsorption energy and activation energy. Notably, due to differences in the order of NH_3 desorption, the dissociative and conservative mechanisms entail NH_3 desorption in the fifth step, whereas in the other two mechanisms, this occurs in the seventh step. In FIG. 6(b), we investigated variations in adsorption energy under different coordination environments to assess catalytic properties. It is evident that

DOI: 10.1063/1674-0068/cjcp2403036

reducing the number of N atoms coordinated with the Mn atom leads to a significant decrease in N_2 adsorption energy in the initial reaction step, which is unfavorable for further reaction progression. Consequently, the MnN_3 configuration within the reaction center demonstrates significantly superior performance compared to MnN_1C_2 and MnN_2C_1 configurations.

To further elucidate the exceptional performance of the MnN_3-graphene model, we conducted a detailed analysis of the Bader charge transfer throughout the reaction process. In FIG. 6(c), we segmented the model into three distinct parts: part 1 comprises the graphene substrate, part 2 represents the potential reaction center MnN_3, and part 3 consists of the N_xH_y molecule. FIG. 6(d) illustrates the charge transfer among these three components under the distal mechanism, with similar trends observed in other mechanisms as depicted in FIG. S2 (SM). In most scenarios, from the adsorption of N_2 to the gradual addition of H atoms, the MnN_3 component exhibits minimal change, primarily serving as a conduit for charge transfer between the graphene substrate and the reactant molecules. This observation further underscores the stability of the catalytic center.

IV. CONCLUSION

In summary, we have systematically studied two graphene-based single-atom MnN_x-graphene ($x=3$, 4) catalysts for nitrogen reduction reaction from first-principles calculations. MnN_3-graphene exhibits excellent catalytic performance via the distal mechanism with a predicted low potential of 0.49 V, which is much lower than previous literature based on $Mn_{SA}@V_S$-N_1, making the NRR reaction easily occur at ambient conditions. More importantly, free energy change in the desorption of NH_3 is only 0.27 eV, ensuring the rapid removal of the produced NH_3 and the stability and durability of MnN_3-graphene. The coordination effect also indicated that single Mn atom coordinated by three N atoms (MnN_3) in the active center possesses superior performance compared to MnN_4, MnN_1C_2 or MnN_2C_1 models.

Supplementary materials: Gibbs free energy diagrams for NRR on MnN_4-graphene model, the E_{ads}(*H) and E_{ads}(*N_2) for MnN_4-graphene and MnN_3-graphene, Gibbs free energy changes for desorption of N_2H_4 and NH_3 on MnN_3-graphene model, the Bader charge variation in different mechanisms and the thermodynamic parameters of related small gas molecules are available.

V. ACKNOWLEDGMENTS

This work was supported by the Excellent Research and Innovation Team Project of Anhui Province (2022AH010001). The density functional theoretical calculations were performed at the High-performance Computing Platform of Anhui University for providing computing resources.

[1] P. Xu, G. Li, Y. Zheng, J. C. H. Fung, A. P. Chen, Z. Z. Zeng, H. Z. Shen, M. Hu, J. F. Mao, Y. Zheng, X. Q. Cui, Z. L. Guo, Y. L. Chen, L. Feng, S. K. He, X. G. Zhang, A. K. H. Lau, S. Tao, and B. Z. Houlton, Nature **626**, 792 (2024).
[2] X. Zhang, E. A. Davidson, D. L. Mauzerall, T. D. Searchinger, P. Dumas, and Y. Shen, Nature **528**, 51 (2015).
[3] J. W. Erisman, M. A. Sutton, J. Galloway, Z. Klimont, and W. Winiwarter, Nat. Geosci. **1**, 636 (2008).
[4] X. B. Fu, J. B. Pedersen, Y. Y. Zhou, M. Saccoccio, S. F. Li, R. Sažinas, K. Li, S. Z. Andersen, A. N. Xu, N. H. Deissler, J. B. V. Mygind, C. Wei, J. Kibsgaard, P. C. K. Vesborg, J. K. Nørskov, and I. Chorkendorff, Science **379**, 707 (2023).
[5] J. W. Erisman, Science **374**, 685 (2021).
[6] V. Smil, Nature **400**, 415 (1999).
[7] X. Y. Niu, S. L. Jiang, and Q. Zhang, Chin. J. Chem. Phys. **34**, 413 (2021).
[8] J. L. Yuan, X. Y. Yi, Y. H. Tang, M. J. Liu, and C. B. Liu, Adv. Funct. Mater. **30**, 1906983 (2020).
[9] H. Iriawan, S. Z. Andersen, X. L. Zhang, B. M. Comer, J. Barrio, P. Chen, A. J. Medford, I. E. L. Stephens, I. Chorkendorff, and Y. Shao-Horn, Nat. Rev. Methods Primers **1**, 56 (2021).
[10] C. Choi, G. H. Gu, J. Noh, H. S. Park, and Y. Jung, Nat. Commun. **12**, 4353 (2021).
[11] P. P. Yu, Y. Wu, H. Yang, M. Xie, W. A. Goddard III, and T. Cheng, Chin. J. Chem. Phys. **36**, 94 (2023).
[12] R. D. Milton, R. Cai, S. Sahin, S. Abdellaoui, B. Alkotaini, D. Leech, and S. D. Minteer, J. Am. Chem. Soc. **139**, 9044 (2017).
[13] B. M. Hoffman, D. Lukoyanov, Z. Y. Yang, D. R. Dean, and L. C. Seefeldt, Chem. Rev. **114**, 4041 (2014).
[14] H. Z. Liu, Chin. J. Catal. **35**, 1619 (2014).
[15] M. A. Shipman and M. D. Symes, Catal. Today **286**, 57 (2017).
[16] S. L. Foster, S. I. P. Bakovic, R. D. Duda, S. Mahesh-

wari, R. D. Milton, S. D. Minteer, M. J. Janik, J. N. Renner, and L. F. Greenlee, Nat. Catal. **1**, 490 (2018).
[17] B. H. R. Suryanto, K. Matuszek, J. Choi, R. Y. Hodgetts, H. L. Du, J. M. Bakker, C. S. M. Kang, P. V. Cherepanov, A. N. Simonov, and D. R. MacFarlane, Science **372**, 1187 (2021).
[18] T. Huang, Z. C. Liu, Y. Zhang, F. X. Wang, J. Wen, C. Y. Wang, M. Hossain, Q. J. Xie, S. Z. Yao, and Y. P. Wu, J. Mater. Chem. A **8**, 13679 (2020).
[19] M. Ahmed, C. Wang, Y. Zhao, C. Sathish, Z. H. Lei, L. Qiao, C. H. Sun, S. B. Wang, J. V. Kennedy, A. Vinu, and J. B. Yi, Small **20**, 2308084 (2024).
[20] C. C. Dong, M. H. Li, and X. J. Han, ACS Sustain. Chem. Eng. **11**, 9036 (2023).
[21] Y. C. Wan, J. C. Xu, and R. T. Lv, Mater. Today **27**, 69 (2019).
[22] Z. Y. Xiong, Y. Xu, A. Y. Bao, W. Sheng, and J. Zhan, ACS Appl. Nano Mater. **7**, 4220 (2024).
[23] B. Fang, X. Wang, S. S. Zhang, L. L. Zhang, R. Zhang, K. Wang, S. Y. Song, and H. J. Zhang, Small 2310268 (2024).
[24] H. Fei, R. Q. Liu, J. Wang, T. Guo, F. Y. Liu, Z. Z. Wu, and D. Z. Wang, Chem. Eng. J. **476**, 146895 (2023).
[25] A. Kaiprathu, P. Velayudham, H. Teller, and A. Schechter, J. Solid State Electrochem. **26**, 1897 (2022).
[26] A. N. Singh, R. Anand, M. Zafari, M. Ha, and K. S. Kim, Adv. Energy Mater. 2304106 (2024).
[27] T. R. Wang, J. C. Li, W. Shu, S. L. Hu, R. H. Ouyang, and W. X. Li, Chin. J. Chem. Phys. **33**, 703 (2020).
[28] Y. Z. Zhang, P. H. Li, Y. N. Ren, Y. He, C. X. Zhang, J. Hu, X. Q. Cao, and M. K. H. Leung, Nanomaterials **13**, 2580 (2023).
[29] H. X. Shi, T. H. Liu, Y. L. Fu, H. Wu, B. Fu, and D. H. Zhang, Chin. J. Chem. Phys. **35**, 443 (2022).
[30] L. J. Arachchige, Y. J. Xu, Z. X. Dai, X. L. Zhang, F. Wang, and C. H. Sun, J. Phys. Chem. C **124**, 15295 (2020).
[31] X. W. Zhai, L. Li, X. Y. Liu, Y. F. Li, J. M. Yang, D. Z. Yang, J. L. Zhang, H. X. Yan, and G. X. Ge, Nanoscale **12**, 10035 (2020).
[32] M. Yan, Z. Y. Guo, Q. G. Li, Z. X. Dai, A. M. Yu, and C. H. Sun, ACS Appl. Nano Mater. **5**, 11270 (2022).
[33] Y. Tang, Y. P. Wang, X. L. Cheng, and H. Zhang, J. Phys. Chem. C **127**, 24574 (2023).
[34] K. Chu, Y. P. Liu, J. Wang, and H. Zhang, ACS Appl. Energy Mater. **2**, 2288 (2019).
[35] M. Majumder, H. Saini, I. Dědek, A. Schneemann, N. R. Chodankar, V. Ramarao, M. S. Santosh, A. K. Nanjundan, Š. Kment, D. Dubal, M. Otyepka, R. Zbořil, and K. Jayaramulu, ACS Nano **15**, 17275 (2021).
[36] X. F. Li, Q. K. Li, J. Cheng, L. L. Liu, Q. Yan, Y. C. Wu, X. H. Zhang, Z. Y. Wang, Q. Qiu, and Y. Luo, J. Am. Chem. Soc. **138**, 8706 (2016).
[37] C. Y. Ling, X. W. Bai, Y. X. Ouyang, A. J. Du, and J. L. Wang, J. Phys. Chem. C **122**, 16842 (2018).
[38] Z. T. Shang, B. Song, H. B. Li, H. Zhang, F. Feng, J. Kaelin, W. L. Zhang, B. B. Xie, Y. W. Cheng, K. Lu, and Q. W. Chen, CCS Chem. **4**, 2115 (2022).
[39] Z. Y. Gao, H. Y. Huang, S. P. Xu, L. L. Li, G. Yan, M. L. Zhao, W. J. Yang, and X. J. Zhao, Mol. Catal. **493**, 111091 (2020).
[40] P. E. Blöchl, Phys. Rev. B **50**, 17953 (1994).
[41] G. Kresse and J. Furthmüller, Comput. Mater. Sci. **6**, 15 (1996).
[42] J. P. Perdew, J. A. Chevary, S. H. Vosko, K. A. Jackson, M. R. Pederson, D. J. Singh, and C. Fiolhais, Phys. Rev. B **46**, 6671 (1992).
[43] J. P. Perdew and Y. Wang, Phys. Rev. B **45**, 13244 (1992).
[44] Y. C. Lin, P. Y. Teng, P. W. Chiu, and K. Suenaga, Phys. Rev. Lett. **115**, 206803 (2015).
[45] W. Zhu, B. Sinkovic, E. Vescovo, C. Tanaka, and J. S. Moodera, Phys. Rev. B **64**, 060403 (2001).
[46] S. Grimme, J. Antony, S. Ehrlich, and H. Krieg, J. Chem. Phys. **132**, 154104 (2010).
[47] J. K. Nørskov, J. Rossmeisl, A. Logadottir, L. Lindqvist, J. R. Kitchin, T. Bligaard, and H. Jónsson, J. Phys. Chem. B **108**, 17886 (2004).
[48] A. A. Peterson, F. Abild-Pedersen, F. Studt, J. Rossmeisl, and J. K. Nørskov, Energy Environ. Sci. **3**, 1311 (2010).
[49] *NIST Chemistry WebBook*, http://webbook.nist.gov/chemistry/.
[50] G. Kresse and J. Furthmüller, Phys. Rev. B **54**, 11169 (1996).
[51] G. Kresse and D. Joubert, Phys. Rev. B **59**, 1758 (1999).
[52] D. W. Ma, Z. P. Zeng, L. L. Liu, X. W. Huang, and Y. Jia, J. Phys. Chem. C **123**, 19066 (2019).
[53] Z. W. Seh, J. Kibsgaard, C. F. Dickens, I. Chorkendorff, J. K. Nørskov, and T. F. Jaramillo, Science **355**, eaad4998 (2017).

DOI: 10.1063/1674-0068/cjcp2403036